

A classical nucleation theory description of active colloid assembly

Gabriel S. Redner,* Caleb G. Wagner,* Aparna Baskaran, and Michael F. Hagan†
Martin Fisher School of Physics, Brandeis University, Waltham, MA, USA.

Non-aligning self propelled particles with purely repulsive excluded volume interactions undergo an athermal motility-induced phase separation into a dilute gas and a dense cluster phase. Here, we use enhanced sampling computational methods and analytic theory to examine the kinetics of formation of the dense phase. Despite the intrinsically nonequilibrium nature of the phase transition, we show that the kinetics can be described using a framework analogous to equilibrium classical nucleation theory, governed by an effective free energy of cluster formation, with identifiable bulk and surface terms. The theory captures the location of the binodal, nucleation rates as a function of supersaturation, and the cluster size distributions below the binodal, while discrepancies in the metastable region reveal additional physics about the early stages of active crystal formation. The success of the theory shows that tools from equilibrium statistical mechanics can provide insights into the kinetics of evolution toward nonequilibrium steady-states in active matter systems.

Active fluids consisting of self-propelled units are present in many biological systems, including the cell cytoplasm [1–3], bacterial suspensions [4–7], and animal flocks [8–11]. Recently, researchers have also developed synthetic active fluids, consisting of chemically [12–17] or electrically [18] propelled colloids, or monolayers of vibrated granular particles [19–22]. Being intrinsically nonequilibrium, active fluids cannot be described by equilibrium statistical mechanics [23, 24] and exhibit behaviors not possible in equilibrium systems, such as spontaneous flow [25–38], anomalous density fluctuations [19, 39], and athermal phase separation [40–50]. Yet, active systems frequently evolve to well-defined time-independent distributions, and in some cases are characterized by equilibrium-like state variables such as temperature or pressure [48, 51–57]. While significant progress has been made toward understanding these stationary distributions, the kinetics of evolution toward steady-state remain poorly understood.

As in equilibrium physics, progress in active matter often stems from simplified model systems. One such system is composed of active Brownian particles (ABPs): self-propelled particles which interact solely by short-range isotropic repulsion. Despite lacking interparticle attractions or alignment interactions, ABPs form macroscopic, crystalline clusters [40–45, 47, 58–60]. ABP phase separation is strikingly reminiscent of equilibrium vapor-liquid systems, with the densities of the coexisting phases falling along a binodal, and critical-like behavior near its apex. As a minimal model system possessing nontrivial phase behavior, ABPs are ideal for studying evolution toward steady-state in generic active systems. However, while the coarsening of deeply quenched ABP clusters has been studied numerically [41, 42, 45], there is no theory for the complete kinetics of phase separation.

In this article, we describe ABP cluster formation dynamics and steady-state phase behavior with a theory

analogous to classical nucleation theory (CNT) for equilibrium phase separation [61–63]. Beginning with the geometry of self-propelled particle interactions, we construct an effective free energy of cluster formation which resembles that of droplet nucleation in an equilibrium liquid-vapor system, including a chemical potential and surface tension. We then apply the framework of CNT to calculate nucleation rates and critical nucleus sizes as functions of particle density and propulsion velocity.

We test the theory against simulations of ABPs, employing enhanced sampling techniques to make systematic measurements of nucleation rates. Despite approximations in our microscopic model, the predicted phase boundary matches simulation results almost quantitatively, with no fitting parameters. Moreover, the predicted and measured cluster size distributions match well below the binodal, though we discuss interesting differences for small clusters that lead to power law scaling. The theory qualitatively predicts the dependence of nucleation rates on super-saturation, although significant quantitative differences are seen near the binodal.

While previous work has developed phenomenological approaches such as Cahn-Hilliard and dynamic density functional theories to describe active colloid athermal phase separation [42, 64–66], here we show how such frameworks directly emerge from the kinetics of the microscopic model. In the last century, CNT drove tremendous advances in the fields of equilibrium crystallization and self-assembly by relating relating particle-scale interactions to their macroscale assembly dynamics. The framework described here moves toward a similar capability in active materials, showing how the breaking of time reversal symmetry at the level of individual particles controls emergent nonequilibrium assembly.

Model. ABPs in two dimensions obey the overdamped Langevin equations:

$$\begin{aligned}\dot{\mathbf{r}}_i &= \mathbf{F}(\{\mathbf{r}_i\})/\xi + v_p \hat{\mathbf{v}}_i + \sqrt{2D}\boldsymbol{\eta}_i^T & (1) \\ \dot{\theta}_i &= \sqrt{2D_r}\eta_i^R. & (2)\end{aligned}$$

Here \mathbf{F} represents the interparticle repulsion force, ξ is the drag, v_p is the magnitude of the self-propulsion ve-

* These authors contributed equally

† hagan@brandeis.edu

locity, and $\hat{\nu}_i = (\cos\theta_i, \sin\theta_i)$. The η variables introduce Gaussian noise, with $\langle \eta_i(t) \rangle = 0$ and $\langle \eta_i(t)\eta_j(t') \rangle = \delta_{ij}\delta(t-t')$. In principle the noise may be nonthermal, but we choose thermal noise with the spatial and rotational diffusion constants given by $D = k_B T/\xi$ and $D_r = \frac{3D}{\sigma^2}$, with σ the particle diameter.

We now represent the instantaneous state of the system by the number density ρ_n of clusters with n particles, and write master equations for their time-evolution (following the approach for equilibrium systems [67])

$$\begin{aligned} \partial_t \rho_n &= J(n-1) - J(n) \\ J(n) &= j_{\text{in}}(n)S(n)\rho_n - j_{\text{out}}(n+1)S(n+1)\rho_{n+1}, \end{aligned} \quad (3)$$

where the fluxes j_{in} and j_{out} represent the rates of monomer gain and loss per unit of cluster surface and $S(n)$ is the surface area (perimeter) of a cluster of size n . We have assumed that the system is well-mixed, and that clusters evolve only by the gain and loss of individual monomers from their perimeters. Our results support these assumptions, except for large clusters in systems with high packing fractions.

We next consider a system at steady-state, so the fluxes J are zero, and solve Eq. 4 for the steady-state cluster size distribution (CSD) $P(n)$:

$$\rho_n = \rho_1 \prod_{m=1}^{n-1} \frac{j_{\text{in}}(m)S(m)}{j_{\text{out}}(m+1)S(m+1)} \equiv \rho_1 P(n), \quad (5)$$

This result is valid for metastable systems (in a quasi-steady state), so long as the time to escape from the metastable state is slow compared to the settling time of the CSD. In this case, ρ_n must be explicitly set to zero above some critical cluster size n_{crit} . While the existence of such a steady-state is not guaranteed in a nonequilibrium system, they are consistently observed in our simulations. Thus, while our microscopic equations of motion violate microscopic reversibility, the system appears to satisfy detailed balance at the level of the coarse variables $\{\rho_n\}$.

Next, we relax the steady-state assumption, but assume that the cluster size distribution remains (quasi) stationary, $\partial_t \rho_n = 0$, so the system satisfies balance rather than the stronger condition of detailed balance. All of the fluxes J are then equal, and given by [68]

$$J = \rho_1 \left(\sum_{n=1}^{\infty} \frac{1}{j_{\text{in}}(n)S(n)P(n)} \right)^{-1}. \quad (6)$$

The mean nucleation time in a system with volume V is then $\tau_{\text{nucl}} = (JV)^{-1}$ [61].

To continue the analogy with CNT, we define an ‘equilibrium’ constant $k_c(n) = \frac{\rho_n v_0}{(\rho_g v_0)^n}$ where v_0 is the standard state volume and ρ_g measures the monomer density in the ‘free volume’ not occupied by clusters. We can then write an effective free energy change for the reaction in which n monomers coalesce into an n -particle cluster:

$$G(n) = -k_B T_{\text{eff}} \ln k_c(n) - n\mu = -k_B T_{\text{eff}} \ln(v_0 \rho_n) \quad (7)$$

where μ is an effective chemical potential (discussed below), and $k_B T_{\text{eff}}$ gives dimensions of energy. The latter’s value need not equal the physical temperature of Eqs. 1 and 2 and does not affect any observables.

Kinetic Theory. Thus far, our formulation is exact. To proceed further, we construct a minimal microscopic model that enables estimating the adsorption and evaporation fluxes from clusters. We model each cluster as circular, with volume $V(n) = n/\rho_c$ and surface area $S(n) = \sqrt{4\pi n/\rho_c}$, comprised of nearly close-packed spheres at number density ρ_c .

To estimate the arrival flux j_{in} , we assume the monomer gas to be homogeneous, isotropic, and composed of particles moving at a single constant speed v_p . We additionally assume $v_p \sigma/D \gg 1$ so we may neglect the effects of translational diffusion. The flux of monomers impinging on a cluster surface is then $j_{\text{in}} = \frac{\rho_g v_p}{\pi}$, independent of cluster size.

For the departure flux, we consider a stationary particle on a cluster surface, with its orientation evolving diffusively. The particle remains on the surface only so long as its propulsion is oriented inwards to the surface, and so we solve the rotational diffusion equation with absorbing boundaries at the ‘horizon’ where propulsion is oriented outwards and the particle escapes. A particle probes the cluster surface over the scale of its own diameter (see Fig. 1), and we therefore estimate the horizon angle as $\alpha(n) = \frac{1}{2} \left(\pi - \sin^{-1} \frac{\sigma}{2r(n)} \right)$. Following the approach of [69], we find $j_{\text{out}}(n) = \frac{D_r}{\sigma} \left(\frac{\pi}{2\alpha(n)} \right)^2$.

Plugging in to Eq. 5, we have:

$$P(n) = \frac{(z\rho_g)^{n-1}}{\sqrt{n}} P_0(n) \quad (8)$$

where $z = \frac{v_p \sigma}{\pi D_r}$ is analogous to the Péclet number, and $P_0(n) = \left[\prod_{m=1}^{n-1} (2\alpha(m+1)/\pi) \right]^2$ accounts for the geometric effects of cluster size.

Results. To gain physical intuition, we use Eqs. 8 and Eq. 7 to obtain the effective free energy of cluster formation:

$$G(n) = -k_B T \left[n \ln(z\rho_g) - \frac{1}{2} \ln(n) + \ln(P_0(n)) \right]. \quad (9)$$

It is evident that the quantity $z\rho_g$ controls the phase behavior of the system, and is analogous to the supersaturation of the fluid phase. As shown in Fig. 1, $G(n)$ is monotonically increasing when $z\rho_g < 1$, corresponding to a homogeneous fluid, while for $1 < z\rho_g < \sqrt{2} \left(\frac{2\alpha(2)}{\pi} \right)^2 \approx 2.42$ it exhibits a barrier followed by a monotonic decrease, corresponding to a supersaturated fluid which is metastable to cluster nucleation. At higher values (beyond the ‘spinodal’), $G(n)$ is monotonically decreasing and the system is unstable towards cluster formation.

For large clusters, P_0 can be simplified to give:

$$G(n) = -k_B T \left[\ln(z\rho_g)n - \frac{\sigma\rho_c}{\pi} S(n) \right] \quad (10)$$

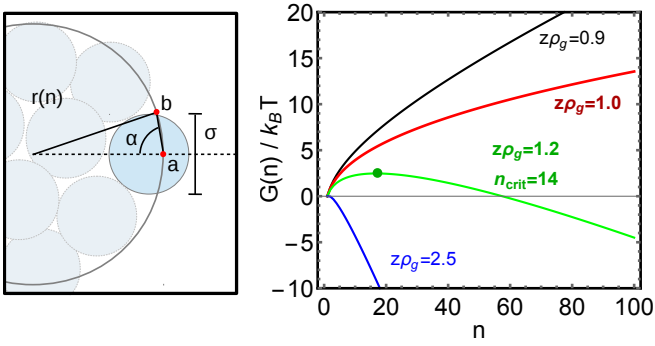


FIG. 1. Left: Depiction of the influence of curvature on the escape horizon. The cluster is approximated as a circle, and points **a** and **b** lie on its boundary, separated vertically by $\sigma/2$. The angle α represents the width of the “horizon” above which a particle’s propulsion must point in order for it to escape. Right: Effective free energy as a function of the supersaturation $z\rho_g$, in the single-phase region (black), at the binodal (red), in the metastable region showing a nucleation barrier (green), and in the spinodal regime (blue).

From this, we see that a geometric understanding of ABP microdynamics leads naturally to their equilibrium-like phase behavior. The first term in Eq.(10) is proportional to the cluster’s volume, and represents the difference in effective chemical potential between the dense and dilute phases; *i.e.*, the chemical potential of the cluster phase is $\mu_c \propto -\ln z$. While μ_c might be interpreted as an effective attraction between particles, extension of the kinetic model to include energetic interparticle attractions shows that the relationship is subtle [69]. The second term is related to the cluster’s surface area, and can be interpreted as a line tension that drives coarsening. This effective line tension is a positive constant, in contrast to a previous result that suggests a negative line tension [66]. Solving $\Delta G(n) = 0$ gives a prediction for the critical nucleus size as $n_{\text{crit}} = \sigma^2 \rho_c / \pi [\ln(z\rho_g)]^2$, a form familiar from classical nucleation theory. We note, however, that even prior to nucleation ρ_g cannot be equated to the total particle density, as is typically assumed in equilibrium CNT. Due to the low effective surface tension of this system, the depletion of monomers by transient sub-critical clusters cannot be neglected.

Next, we demonstrate that, despite its simplifications, the theory provides quantitative insights into ABP systems. Our simulations are performed as in [41] (see [68] for details), though to measure nucleation times much larger than those accessible in brute force simulations, we used the weighted-ensemble dynamics method [70–72]. To compare the theory and simulations, we must express the theoretical gas density ρ_g in terms of the overall volume fraction ϕ , since the latter is the control parameter in our NVT simulations. We do so via the coordinate transformation [68]

$$\phi = \frac{A\rho_c}{(4/\pi\sigma^2)A - 1 + \rho_c/\rho_g} \quad (11)$$

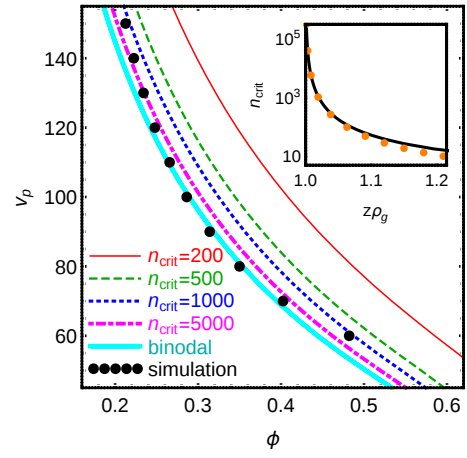


FIG. 2. Plot of the binodal and several iso-critical lines as computed from our kinetic theory. Black dots denote the location of the binodal as measured from simulations, showing remarkable agreement with the parameter-free theoretical prediction. Inset shows the critical nucleus size diverging as $z\rho_g \rightarrow 1$, with good agreement between the exact calculation (black line) and the approximate form derived in the main text (orange points).

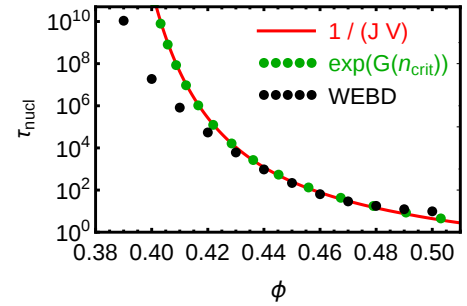


FIG. 3. Mean nucleation times as computed from the full kinetic expression (Eq. 6, red), and by applying an Arrhenius form to the height of the nucleation barrier (Eq. 9, green). The latter approach does not supply the kinetic prefactor, which must be determined by fitting. Nucleation rates as measured by weighted ensemble dynamics simulations are shown in black.

where $A = \frac{\pi\sigma^2}{4} \sum_{n=1}^{n_{\text{max}}} nP(n)$ with n_{max} the cutoff cluster size [68]. To make quantitative comparisons with simulation, we also use an empirical form for density within large clusters, $\rho_c(v_p)$, which increases with propulsion speed due to the imperfectly hard interaction potential [68]. The resulting phase diagram is shown in Fig. 2. The predicted binodal is remarkably close to its measured location, although this could be partly fortuitous.

We now employ Eqs. (11) and (6) to compute the mean nucleation time in the metastable regime. Here we find that the parameter-free theory lacks quantitative accuracy, primarily because the predicted nucleation rate is exquisitely sensitive to small perturbations of $z\rho_g$. To enable qualitative comparisons, we set $\rho_g^{\text{eff}} = \chi\rho_g$, with χ a fitting parameter which adjusts the monomer chemical

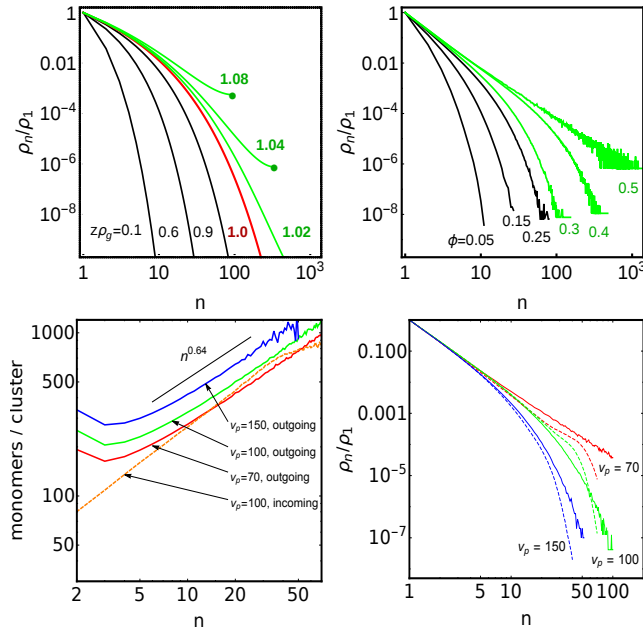


FIG. 4. Top: Cluster size distributions (CSDs), as predicted by Eq. 5 (left) and as measured in simulations for $v_p = 100$ (right). Data are colored based on their location in the phase diagram: black for single-phase, red at the binodal, and green in the metastable regime. Bottom left: Comparison of incoming and outgoing rates for various values of v_p above the binodal, with $z\rho_g = 1.04$. The rates shown are integrated over the cluster surface and then averaged over the ensemble of clusters with size n ; hence, the units are (monomers/cluster). Bottom right: Comparison of the CSDs at $z\rho_g = 1.04$ from simulations (solid) and as reconstructed from the simulated rates (dashed).

potential. We find (by eye) that setting $\chi = 0.71$ produces good correspondence with simulation (Fig. 3). Nucleation rates are notoriously difficult to quantitatively predict from first principles even in the equilibrium case (*e.g.* [73–77]), and so the correspondence between theory and simulation with a single small fitting parameter is notable.

Finally, we compare the theoretical and simulated CSDs in Fig. 4. Below the binodal, the theory captures the functional form of the CSDs, but in the metastable region fails to account for a power law scaling $\rho_n \propto n^{-2}$ below a threshold cluster size. This discrepancy stems in part from treating clusters as spherical. Though this description captures many features of the phase separation kinetics, to understand the full CSDs the complex geometric structure of the clusters is not ignorable. In particular, simulations show clusters with ramified structure and fractal surface area scaling $S(n) \sim n^{0.64 \pm 0.01}$ [68]. In this case the outgoing flux retains its basic form, but must be averaged over cluster morphologies [68]:

$$\overline{j_{\text{out}}}(n) \equiv \frac{\langle \oint_{S_c} j_{\text{out}}(n, s) ds \rangle}{\langle S(n) \rangle} = \frac{D_r}{\sigma} + \frac{2D_r}{\langle S(n) \rangle}, \quad (12)$$

where S_c denotes a cluster surface and angled brackets an ensemble average. Thus, we expect the outgoing rate to scale with $\langle S(n) \rangle$ to leading order.

Directly measuring the rates confirms deviation from the $n^{1/2}$ scaling expected for spherical clusters (Fig. 4). Moreover, simulated rates are larger than predicted by the theory, with the outgoing rates depending on v_p . This also results from the complex cluster geometry: on small clusters or near regions of high curvature, particles can escape by “sliding off” each other before completely rotating to the horizon, thus resulting in a higher than predicted, v_p -dependent outgoing rate. Multi-particle escape events may also contribute [41]. As an additional verification, we fed the measured rates into Eq. 5 to reconstruct the CSDs, which showed good agreement with simulation (Fig. 4). Similar results were obtained elsewhere in the phase diagram (see [68]). Thus, a more detailed calculation of the rates should recover the scaling of simulated CSDs. We may consider as an equilibrium analogue the Fisher droplet model [78], which shows that accounting for the entropic contribution of cluster surface fluctuations leads to a power law in the CSD near the critical point, with the exponent $31/15 \approx 2.066$ for the 2D Ising universality class. (However, [79] obtains an exponent of 1.70 ± 0.05 for a different active matter model.) Interestingly, the above discussion suggests that accounting for interactions between clusters is not necessary to explain the existence of power law scaling in CSDs.

In summary, we have shown that an approach analogous to classical nucleation theory can describe the nonequilibrium nucleation of clusters from solutions of ABPs. By linking the microscopic parameters of ABPs to their macroscale kinetics, this framework makes an important step toward developing design principles for applications of motility-induced phase separation.

While completing this manuscript, we learned of another concurrent study which computationally measures ABP nucleation rates [80]. By analyzing simulation trajectories, they conclude that cluster size and cluster polarization (the extent to which particles on the rim of a cluster point inwards) are important collective coordinates for describing transition rates. These observations are consistent with the kinetic theory described here.

Acknowledgments. This work was supported by the NSF (DMR-1149266 and the Brandeis MRSEC DMR-1420382). Computational resources were provided by the NSF through XSEDE computing resources and the Brandeis HPCC.

I. A CLASSICAL NUCLEATION THEORY DESCRIPTION OF ACTIVE COLLOID ASSEMBLY
SUPPLEMENTARY MATERIALS

A. Simulation Details

To validate the predicted cluster size distributions (CSDs) and phase diagram, we performed Brownian dynamics simulations identical to those in [41]. To measure the CSDs, we performed simulations with $N = 30000$ particles, run for 200τ . Particles are considered to be bonded if their separation is less than σ , and clusters are identified as groups of bonded particles [41, 69]. We ran five simulations at each parameter set, discarded the first 1τ of each trajectory, and averaged the results. We also discarded frames in which any cluster containing more than 1500 particles existed, to exclude phase-separated configurations.

To locate the binodal, we ran similar simulations until 400τ and measured the density of the dilute phase, averaging over ten separate simulations. In configurations where clusters existed, we separately measured the density of the cluster interior (discarding the edge region) and the density of the dilute phase (discarding the cluster and surrounding boundary region). The empirical form for ρ_c was determined in conjunction with these simulations. As shown in Fig. 5, the density of the cluster interior was tabulated for various values of v_p and the resulting trend fit to the functional form

$$\rho_c \approx 1.1322 + \sqrt{0.00199v_p - 0.08788}. \quad (13)$$

Measurement of nucleation rates in simulations. The rates of nucleation were determined using the weighted-ensemble (WEBD) method [70–72], which allows for precise rate measurement of extremely rare events and is applicable to non-equilibrium dynamics. We performed the calculation on systems of size $N = 15000$ and used the size of the largest cluster as our progress coordinate. At the first appearance of a cluster of size n_0 (usually chosen to be a few thousand), a system was considered to have undergone a nucleation event. In practice, this amounted running each ensemble for about 160 and 2000 WEBD iterations, depending on the rate of convergence. The bin boundaries were calculated separately for each WEBD run using the procedure outlined in Ref. [70], Appendix C

B. Calculation of Nucleation Rate

We assume the cluster size distribution remains (quasi) stationary, such that $\partial_t \rho_n = 0$ and therefore $J(n) = J$, where J is a constant. Using the definition of $J(n)$, this implies

$$\rho_{n+1} - b_n \rho_n = -\frac{J}{j_{\text{out}}(n+1)S(n+1)}. \quad (14)$$

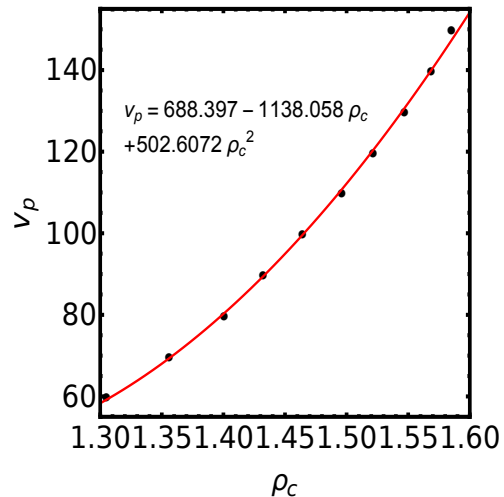


FIG. 5. Cluster densities ρ_c as a function of Peclet number for phase-separated systems on the binodal. Inversion of the quadratic fit (red) gives Eq. 13.

where $b_n \equiv \frac{j_{\text{in}}(n)S(n)}{j_{\text{out}}(n+1)S(n+1)}$. Now dividing both sides by $\prod_{m=1}^n b_m$, we get:

$$\frac{\rho_{n+1}}{\prod_{m=1}^n b_m} - \frac{\rho_n}{\prod_{m=1}^{n-1} b_m} = -\frac{J}{j_{\text{in}}(n)S(n) \prod_{m=1}^{n-1} b_m}. \quad (15)$$

Summing from $n = 1$ to an arbitrary cutoff $n = N - 1$ gives

$$\frac{\rho_N}{\prod_{m=1}^{N-1} b_m} - \rho_1 = -J \sum_{n=1}^{N-1} \frac{1}{j_{\text{in}}(n)S(n) \prod_{m=1}^{n-1} b_m}. \quad (16)$$

As $N \rightarrow \infty$, $\rho_N \rightarrow 0$. Taking this limit, and also recognizing that $\prod_{m=1}^{n-1} b_m = P(n)$, we obtain

$$\rho_1 = J \sum_{n=1}^{\infty} \frac{1}{j_{\text{in}}(n)S(n)P(n)}. \quad (17)$$

And so

$$J = \rho_1 \left(\sum_{n=1}^{\infty} \frac{1}{j_{\text{in}}(n)S(n)P(n)} \right)^{-1}. \quad (18)$$

C. Calculation of j_{out} for non-spherical clusters

The quantity of interest is the ensemble averaged outgoing flux, $\overline{j_{\text{out}}}(n)$:

$$\overline{j_{\text{out}}}(n) \equiv \frac{1}{\langle S(n) \rangle} \left\langle \oint_{S_c} j_{\text{out}}(n, s) ds \right\rangle, \quad (19)$$

where $j_{\text{out}}(n, s)$ is the local outgoing flux on a cluster surface S_c parametrized by s , and angled brackets denote an average over the ensemble of clusters of size n . For an arbitrary point on S_c (excluding the degenerate case

of 0 curvature) there is a unique osculating circle whose radius $r(n, s)$ defines the curvature $k(n, s)$ at that point:

$$r(n, s) = \frac{1}{|k(n, s)|}. \quad (20)$$

The absolute value can be removed provided we define a signed “radius” $r_{\text{sgn}}(n, s)$ that matches the sign of the curvature:

$$r_{\text{sgn}}(n, s) = \frac{1}{k(n, s)}. \quad (21)$$

The same calculation employed in the main text to calculate the outgoing rate on a spherical clusters applies *locally* on S_c , provided we take for our “radius” the quantity $r_{\text{sgn}}(n, s)$. Using the result from the main text, this allows us to write

$$\oint_{S_c} j_{\text{out}}(n, s) ds = \frac{\pi^2 D_r}{4 \sigma} \oint_{S_c} \left[\frac{1}{2} \left(\pi - \arcsin \left(\frac{\sigma}{2r_{\text{sgn}}(n, s)} \right) \right) \right]^{-2} ds. \quad (22)$$

To proceed further, we make the following approximation: Clusters with regions of high curvature (such that $r_{\text{sgn}}(n, s)$ is smaller than or on the order of σ) are improbable. With this assumption we can expand the integrand to obtain

$$\oint_{S_c} j_{\text{out}}(n, s) ds \simeq \frac{\pi^2 D_r}{4 \sigma} \left[\frac{4}{\pi^2} S(n) + \frac{4\sigma}{\pi^3} \oint_{S_c} k(n, s) ds \right]. \quad (23)$$

The second integral may be evaluated using the Gauss-Bonnet theorem: for the topology of a disk, $\oint k(n, s) ds = 2\pi$. Therefore,

$$\oint_{S_c} j_{\text{out}}(n, s) ds = \frac{D_r}{\sigma} S(n) + 2D_r. \quad (24)$$

Referring back to Eq. 19, we then obtain

$$\overline{j_{\text{out}}}(n) = \frac{D_r}{\sigma} + \frac{2D_r}{\langle S(n) \rangle}. \quad (25)$$

D. Surface Area Scaling

We formalize the measure of cluster surface area using the notion of an α -shape, which defines a concave hull of a set of points with respect to the spatial resolution α [81]. By replacing each monomer with a constellation of points on its surface and taking α to be the monomer radius, the α -shape corresponds to the physically relevant cluster surface. We performed the calculation using the α -shape algorithm from the Computational Geometry Algorithms Library (CGAL), on configurations from the simulations used to measure the cluster size distributions. The surface area for clusters of each size n was

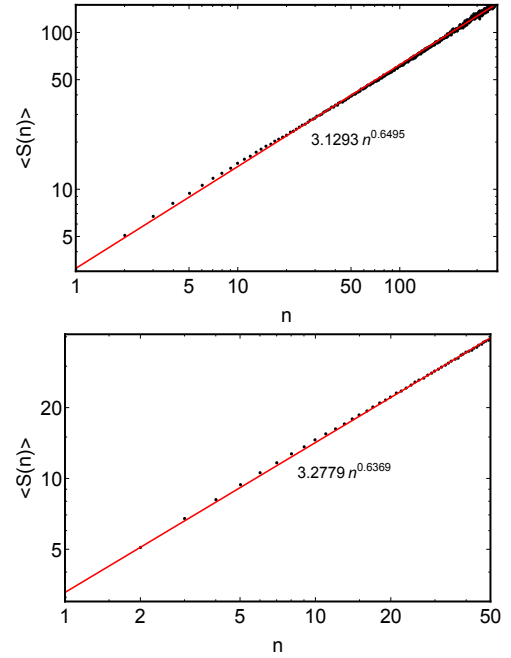


FIG. 6. Two examples of the power law fits used to determine the surface area scaling. Red denotes the power law fit, and black circles the simulation data. Both plots were measured from simulations on the binodal, with $(v_p, \phi) = (50, 0.502)$ [top] and $(v_p, \phi) = (100, 0.289)$ [bottom].

averaged over the entire simulation, and the resulting distribution was fit to a power law (Fig. 6). A random error of ± 0.0013 was obtained by running 16 simulations at the same point in phase space ($v_p = 100, \phi = 0.29$) and taking the standard deviation of the measured scaling exponent. Somewhat larger variations of about ± 0.01 were observed as v_p and ϕ were varied independently, but without any obvious trend. Since such small variations are irrelevant for our purposes, we take for the scaling exponent the overall average 0.64 ± 0.01 .

E. Measurement of evaporation and adsorption rates

To measure evaporation and adsorption rates, simulations were performed as described in Section I, but without translational diffusion in order to avoid counting events in which a monomer rapidly leaves and rejoins a cluster. This is justified since we are working in the regime where $v_p \sigma / D \gg 1$, such that any true evaporation or adsorption event is unlikely to be caused by translational diffusion. Each simulation was run until 10τ , with the first 1τ of data discarded. To measure rates, a small time interval $\Delta t = 0.0001\tau$ was considered, during which the probability of two evaporation or adsorption events occurring simultaneously on the same cluster is low. If a monomer was identified which Δt units previously was located on the boundary of a cluster of size n , one evapo-

ration event for that value of n was counted. Conversely, if a cluster of size n was found with x monomers on its boundary that previously did not belong to a cluster, x adsorption events were counted. The number of events was then summed to obtain average rates for each cluster size. Results are given in Fig. 7 for $z\rho_g = 0.6$ and $z\rho_g = 1$ (the binodal), together with a direct comparison to the rates predicted by the kinetic theory on the binodal. Finally, the rates were inputted into the kinetic theory from the main text in order to reconstruct the CSDs. These results are presented in Fig. 8, showing good agreement with simulation.

Effects of cluster-cluster interactions. While the CSDs computed from the measured rates fit the simulation CSDs very well for small and moderate cluster sizes, they begin to deviate in the limit of large clusters. This deviation likely arises because, for sufficiently high system densities, the growth of large clusters is no longer dominated by single monomer adsorption, as is assumed in our theory. More precisely, we must consider the general class of reaction pathways in which clusters of sizes k and $n - k$ combine to form a cluster of size n , and k may range from 1 to $\lfloor n/2 \rfloor$. For large clusters in dense systems, it may no longer be reliable to ignore all reaction pathways in which $k \neq 1$. Thus, while not directly responsible for the appearance of power law scaling in the CSDs, cluster interactions appear to influence the location of the threshold size characterizing the crossover from power law scaling to exponential decay. Indeed, it is surprising that our model, which assumes non-interacting clusters, works as well as it does in the high density region.

F. Derivation of the Coordinate Transformation

By definition of the overall volume fraction ϕ ,

$$\phi = \frac{\pi\sigma^2}{4} \sum_{n=1}^{n_{\max}} n\rho_n \quad (26)$$

In single phase regime or at the binodal, the sum in (26) rigorously should be extended to ∞ . However, for purposes of numerical calculation, a sufficiently accurate estimate is achieved for $n_{\max} = 1000$. In the metastable regime we assume that nucleation has not yet occurred, such that terms with large enough n do not contribute to the sum. In practice, we enforce this constraint by setting $n_{\max} = \min(n_{\text{crit}}, 1000)$. Inserting the expression for the cluster size distribution, we get

$$\phi = \frac{\pi\sigma^2}{4} \sum_{n=1}^{n_{\max}} n\rho_1 P(n) \quad (27)$$

$$= \frac{\pi\sigma^2}{4} \sum_{n=1}^{n_{\max}} n\rho_1 \frac{(z\rho_g)^{n-1}}{\sqrt{n}} P_0(n) \quad (28)$$

To eliminate the unknown monomer density, ρ_1 , we make use of the definition of ρ_g , which can be written as the

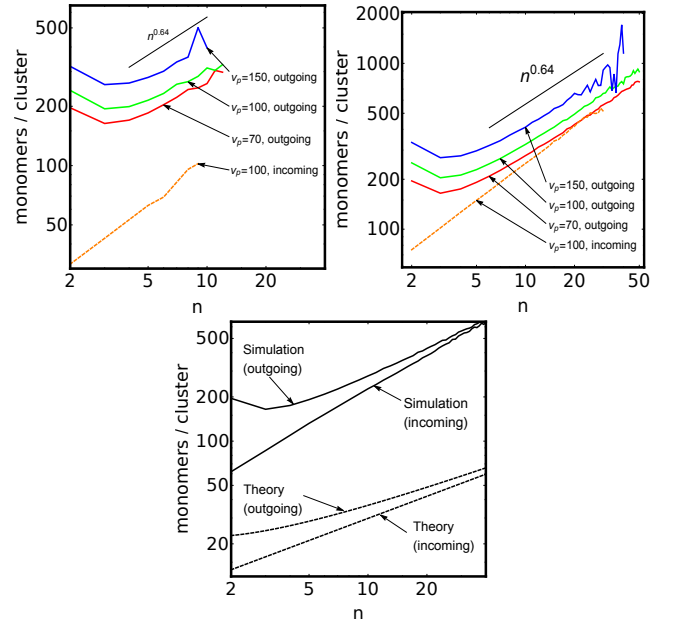


FIG. 7. Top left: Comparison of incoming and outgoing rates for various values of v_p below the binodal, with $z\rho_g = 0.6$. The rates shown are integrated over the cluster surface and then averaged over the ensemble of clusters with size n ; hence, the units are (monomers/cluster). Top right: Same as on the left, except on the binodal ($z\rho_g = 1$). Bottom: Comparison of rates on the binodal from simulations (solid black) and as computed by the kinetic theory (dashed black). The theoretical rates are integrated with respect to surface area scaling $S(n) = \pi n^{1/2}$.

number of monomers divided by the ‘free volume’ unoccupied by other clusters:

$$\rho_g = \frac{\rho_1 V}{V - \sum_{n=2}^{n_{\max}} V(n) \rho_n V} \quad (29)$$

with V the total system volume and $V(n)$ the volume of a cluster with size n . Solving for ρ_1 and substituting into (28) gives

$$\phi = \frac{\pi\sigma^2}{4} \sum_{n=1}^{n_{\max}} \frac{\sqrt{n} (z\rho_g)^n P_0(n)}{z} \left(1 - \rho_1 \sum_{m=2}^{n_{\max}} V(m) P(m) \right) \quad (30)$$

It appears that no progress has been made since ϕ is again given in terms of the unknown ρ_1 . However, from (27) we see that

$$\rho_1 = \frac{4\phi}{\pi\sigma^2} \left[\sum_{n=1}^{n_{\max}} nP(n) \right]^{-1}. \quad (31)$$

By substitution into (30) we can therefore eliminate ρ_1 and self-consistently solve for ϕ :

$$\phi = \frac{B}{BC + z} \quad (32)$$

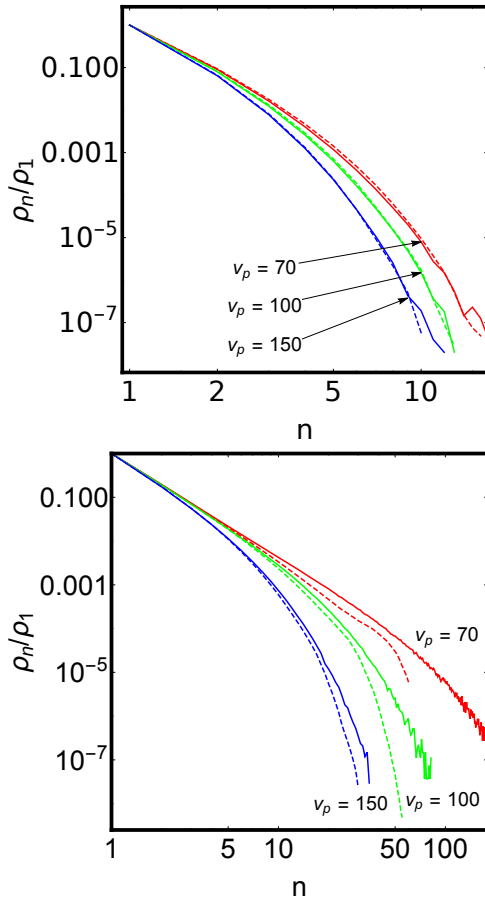


FIG. 8. Top: Cluster size distributions (CSDs) below the binodal, with $z\rho_g = 0.6$. The simulated CSDs are solid red, green, and blue. The CSDs determined by feeding directly measured rates into Eq. 5 in the main text are dashed red, green, and blue. Bottom: Same as on the top, except at the binodal ($z\rho_g = 1$).

where

$$B = \frac{\pi\sigma^2 z\rho_g}{4} \sum_{n=1}^{n_{\max}} nP(n) \quad (33)$$

$$C = \frac{4}{\pi\sigma^2} \left[\sum_{n=1}^{n_{\max}} nP(n) \right]^{-1} \sum_{n=2}^{n_{\max}} V(n)P(n) \quad (34)$$

Finally, using $V(n) = n/\rho_c$ and the definition of $P(n)$, this can be rearranged to read

$$\phi = \frac{A\rho_c}{(4/\pi\sigma^2)A - 1 + \rho_c/\rho_g} \quad (35)$$

where $A = \frac{\pi\sigma^2}{4} \sum_{n=1}^{n_{\max}} nP(n)$.

The transformation for v_p follows trivially from the definition of z :

$$v_p = \frac{\pi D_r}{\sigma} z. \quad (36)$$

-
- [1] J. Brugués, V. Nuzzo, E. Mazur, and D. J. Needleman, *Cell* **149**, 554 (2012).
 - [2] J. Brugués and D. Needleman, *Proc. Natl. Acad. Sci. U. S. A.* **111**, 18496 (2014).
 - [3] R. E. Goldstein and J.-W. van de Meent, *Interface Focus* **5**, 20150030 (2015).
 - [4] L. Cisneros, J. Kessler, S. Ganguly, and R. Goldstein, *Phys. Rev. E* **83**, 061907 (2011).
 - [5] C. Dombrowski, L. Cisneros, S. Chatkaew, R. E. Goldstein, and J. O. Kessler, *Phys. Rev. Lett.* **93**, 098103 (4 pages) (2004).
 - [6] A. Kaiser, A. Peshkov, A. Sokolov, B. ten Hagen, H. Lwen, and I. S. Aranson, *Phys. Rev. Lett.* **112**, 158101 (2014).
 - [7] J. Dunkel, S. Heidenreich, K. Drescher, H. H. Wensink, M. Bär, and R. E. Goldstein, *Phys. Rev. Lett.* **110**, 228102 (2013).
 - [8] A. Attanasi, A. Cavagna, L. D. Castello, I. Giardina, T. S. Grigera, A. Jelić, S. Melillo, L. Parisi, O. Pohl, E. Shen, and M. Viale, *Nat. Phys.* **10**, 691 (2014).
 - [9] A. Attanasi, A. Cavagna, L. Del Castello, I. Giardina, S. Melillo, L. Parisi, O. Pohl, B. Rossaro, E. Shen, E. Silvestri, and M. Viale, *PLoS Comput. Biol.* **10**, e1003697 (2014).
 - [10] E. Shaw, *Amer. Sci.* **66**, 166 (1978).
 - [11] B. Hölldobler and E. O. Wilson, *Journey to the Ants: A Story of Scientific Exploration* (Belknap Press of Harvard University Press, 1994).
 - [12] J. Palacci, C. Cottin-Bizonne, C. Ybert, and L. Bocquet, *Phys. Rev. Lett.* **105**, 088304 (2010).
 - [13] W. F. Paxton, K. C. Kistler, C. C. Olmeda, A. Sen, S. K. St Angelo, Y. Cao, T. E. Mallouk, P. E. Lammert, and V. H. Crespi, *J. Am. Chem. Soc.* **126**, 13424 (2004).
 - [14] Y. Hong, N. Blackman, N. Kopp, A. Sen, and D. Velegol, *Phys. Rev. Lett.* **99**, 178103 (2007).
 - [15] H.-R. Jiang, N. Yoshinaga, and M. Sano, *Phys. Rev. Lett.* **105**, 268302 (2010).
 - [16] G. Volpe, I. Buttinoni, D. Vogt, H.-J. Kümmerer, and C. Bechinger, *Soft Matter* **7**, 8810 (2011).
 - [17] S. Thutupalli, R. Seemann, and S. Herminghaus, *New*

- Journal of Physics* **13**, 073021 (2011).
- [18] A. Bricard, J.-B. Caussin, N. Desreumaux, O. Dauchot, and D. Bartolo, *Nature* **503**, 95 (2013).
- [19] V. Narayan, S. Ramaswamy, and N. Menon, *Science* **317**, 105 (2007).
- [20] A. Kudrolli, G. Lumay, D. Volfson, and L. S. Tsimring, *Phys. Rev. Lett.* **100**, 058001 (2008).
- [21] J. Deseigne, O. Dauchot, and H. Chaté, *Phys. Rev. Lett.* **105**, 098001 (2010).
- [22] N. Kumar, H. Soni, S. Ramaswamy, and A. K. Sood, *Nat Commun* **5** (2014), 10.1038/ncomms5688.
- [23] M. C. Marchetti, J. F. Joanny, S. Ramaswamy, T. B. Liverpool, J. Prost, M. Rao, and R. A. Simha, *Reviews of Modern Physics* **85**, 1143 (2013).
- [24] C. Bechinger, R. D. Leonardo, H. Lowen, C. Reichhardt, G. Volpe, and G. Volpe, [arXiv:1602.00081](https://arxiv.org/abs/1602.00081) (2016).
- [25] M. B. Wan, C. J. Olson Reichhardt, Z. Nussinov, and C. Reichhardt, *Phys. Rev. Lett.* **101**, 018102 (2008).
- [26] J. Tailleur and M. E. Cates, *Europhys. Lett.* **86**, 60002 (2009).
- [27] L. Angelani, A. Costanzo, and R. D. Leonardo, *Europhys. Lett.* **96**, 68002 (2011).
- [28] P. K. Ghosh, V. R. Misko, F. Marchesoni, and F. Nori, *Phys. Rev. Lett.* **110**, 268301 (2013).
- [29] B.-q. Ai, Q.-y. Chen, Y.-f. He, F.-g. Li, and W.-r. Zhong, *Phys. Rev. E* **88**, 062129 (2013).
- [30] L. Giomi, L. Mahadevan, B. Chakraborty, and M. F. Hagan, *Phys. Rev. Lett.* **106**, 218101 (2011).
- [31] L. Giomi and M. C. Marchetti, *Soft Matter* **8**, 129 (2012).
- [32] L. Giomi, L. Mahadevan, B. Chakraborty, and M. F. Hagan, *Nonlinearity* **25**, 2245 (2012).
- [33] R. Voituriez, J. Joanny, and J. Prost, *Phys. Rev. Lett.* **96**, 028102 (2006).
- [34] D. Marenduzzo, E. Orlandini, and J. Yeomans, *Phys. Rev. Lett.* **98**, 118102 (2007).
- [35] H. Chaté, F. Ginelli, and R. Montagne, *Phys. Rev. Lett.* **96**, 180602 (2006).
- [36] S. M. Fielding, D. Marenduzzo, and M. E. Cates, *Phys. Rev. E* **83**, 041910 (2011).
- [37] D. Marenduzzo, E. Orlandini, M. Cates, and J. Yeomans, *J. Non-Newtonian Fluid Mech.* **149**, 56 (2008).
- [38] L. Giomi, M. Marchetti, and T. Liverpool, *Phys. Rev. Lett.* **101**, 198101 (2008).
- [39] S. Ramaswamy, R. A. Simha, and J. Toner, *Europhys. Lett.* **62**, 196 (2003).
- [40] Y. Fily and M. C. Marchetti, *Phys. Rev. Lett.* **108**, 235702 (2012).
- [41] G. S. Redner, M. F. Hagan, and A. Baskaran, *Phys. Rev. Lett.* **110**, 055701 (2013).
- [42] J. Stenhammar, A. Tiribocchi, R. J. Allen, D. Marenduzzo, and M. E. Cates, *Phys. Rev. Lett.* **111**, 145702 (2013).
- [43] I. Buttinoni, J. Bialké, F. Kümmel, H. Löwen, C. Bechinger, and T. Speck, *Phys. Rev. Lett.* **110**, 238301 (2013).
- [44] B. M. Mognetti, S. A., S. Angioletti-Uberti, A. Cacciuto, C. Valeriani, and D. Frenkel, *Phys. Rev. Lett.* **111**, 245702 (2013).
- [45] J. Stenhammar, D. Marenduzzo, R. J. Allen, and M. E. Cates, *Soft Matter* **10**, 1489 (2014).
- [46] A. Wysocki, R. G. Winkler, and G. Gompper, *Europhys. Lett.* **105**, 48004 (2014).
- [47] M. E. Cates and J. Tailleur, *Annu. Rev. Condens. Matter Phys.* **6**, 219 (2015), <http://dx.doi.org/10.1146/annurev-conmatphys-031214-014710>.
- [48] M. C. Marchetti, Y. Fily, S. Henkes, A. Patch, and D. Yllanes, *arXiv preprint arXiv:1510.00425* (2015).
- [49] J. Stenhammar, R. Wittkowski, D. Marenduzzo, and M. E. Cates, *Phys. Rev. Lett.* **114**, 018301 (2015).
- [50] R. Ni, M. a. C. Stuart, M. Dijkstra, and P. G. Bolhuis, *Soft Matter* **10**, 6609 (2013).
- [51] A. P. Solon, J. Stenhammar, R. Wittkowski, M. Kardar, Y. Kafri, M. E. Cates, and J. Tailleur, *Phys. Rev. Lett.* **114**, 198301 (2015).
- [52] a. P. Solon, Y. Fily, A. Baskaran, M. E. Cates, Y. Kafri, M. Kardar, and J. Tailleur, *Nat. Phys.* , 4 (2015).
- [53] S. C. Takatori, W. Yan, and J. F. Brady, *Phys. Rev. Lett.* **113**, 028103 (2014).
- [54] S. C. Takatori and J. F. Brady, *Physical Review E* **91**, 032117 (2015).
- [55] T. Speck and R. L. Jack, *arXiv preprint arXiv:1512.00830* (2015).
- [56] T. Speck, A. M. Menzel, J. Bialké, and H. Löwen, *J. Chem. Phys.* **142**, 224109 (2015).
- [57] R. G. Winkler, A. Wysocki, and G. Gompper, (2015), [arXiv:arXiv:1506.03941](https://arxiv.org/abs/1506.03941).
- [58] J. Bialké, T. Speck, and H. Löwen, *J. Non-Cryst. Solids* **407**, 11 (2014).
- [59] M. E. Cates and J. Tailleur, *Annu. Rev. Condens. Matter Phys.* **6**, 150112144536003 (2014).
- [60] A. Wysocki, R. G. Winkler, and G. Gompper, “Cooperative motion of active brownian spheres in three-dimensional dense suspensions,” (2013).
- [61] D. W. Oxtoby, *J. Phys.: Condens. Matter* **4**, 7627 (1999).
- [62] V. Agarwal and B. Peters, “Solute precipitate nucleation: A review of theory and simulation advances,” in *Advances in Chemical Physics: Volume 155* (John Wiley & Sons, Inc., 2014) pp. 97–160.
- [63] J. J. D. Yoreo and P. G. Vekilov, (2003).
- [64] R. Wittkowski, A. Tiribocchi, J. Stenhammar, R. J. Allen, D. Marenduzzo, and M. E. Cates, *Nat. Comm.* **5**, 4351 (2014).
- [65] T. Speck, J. Bialké, A. M. Menzel, and H. Löwen, *Phys. Rev. Lett.* **112**, 218304 (2014).
- [66] J. Bialké, J. T. Siebert, H. Löwen, and T. Speck, *Phys. Rev. Lett.* **115**, 098301 (2015).
- [67] R. Becker and W. Döring, *Ann. Phys. (Leipzig)* **416**, 719 (1935).
- [68] (Supplementary Information), supplemental figures and additional model details are included at the end of this document.
- [69] G. S. Redner, A. Baskaran, and M. F. Hagan, *Phys. Rev. E* **88**, 012305 (2013).
- [70] G. A. Huber and S. Kim, *Biophys. J.* **70**, 97 (1996).
- [71] B. W. Zhang, D. Jasnow, and D. M. Zuckerman, *J. Chem. Phys.* **132**, (2010).
- [72] B. W. Zhang, D. Jasnow, and D. M. Zuckerman, *Proc. Natl. Acad. Sci. U. S. A.* **104**, 18043 (2007).
- [73] S. Auer and D. Frenkel, *Nature* **409**, 1020 (2001), 10.1038/35059035.
- [74] S. Prestipino, A. Laio, and E. Tosatti, *Phys. Rev. Lett.* **108**, 225701 (2012).
- [75] T. D. Loeffler, D. E. Henderson, B. Chen, T. D. Loeffler, D. E. Henderson, and B. Chen, *J. Chem. Phys.* **137**, 19430 (2013).
- [76] A. Statt, P. Virnau, and K. Binder, *Phys. Rev. Lett.* **114**, 26101 (2015).
- [77] R. McGraw, A. Laaksonen, and R. McGraw, *J. Chem.*

[Phys.](#) **106**, 5284 (1997).

[78] M. E. Fisher, *Physics* **3**, 255 (1967).

[79] D. Levis and L. Berthier, [Phys. Rev. E](#) **89**, 062301 (2014).

[80] D. Richard, H. Lowen, and T. Speck, [arXiv:1602.07580](#)

(2016).

[81] H. Edelsbrunner, D. G. Kirkpatrick, and R. Seidel, *Information Theory, IEEE Transactions on* **29**, 551 (1983).